Supporting Information for

Global evolution and dynamics of the geomagnetic field in the 15–70 kyr period based on selected paleomagnetic sediment records

Sanja Panovska[1], Monika Korte[1], Jiabo Liu[2], and Norbert Nowaczyk[3]

[1]GFZ German Research Centre for Geosciences, Section 2.3, Helmholtz Centre Potsdam, Potsdam, Germany
[2]Department of Ocean Science and Engineering, Southern University of Science and Technology, Shenzhen, China
[3]GFZ German Research Centre for Geosciences, Section 4.3, Helmholtz Centre Potsdam, Potsdam, Germany

S1 Conversion of RPI to absolute paleointensity

To convert sedimentary relative paleointensity (RPI) to absolute field intensity (F), first a relative virtual axial dipole moment (rVADM) is calculated based on sedimentary RPI values. Since F and RPI are latitude dependent, this conversion allows the use of more absolute data (global datasets) for calibrating the latitude-independent rVADM. The rVADM is defined as:

$$rVADM = \frac{4\pi r^3}{\mu_0} RPI \sqrt{1 + 3\ cos^2\left(\frac{\pi}{2} - \lambda_S\right)} \tag{S1}$$

where r is the Earth's radius, μ_0 is the magnetic vacuum permeability, λ_S is the geographic latitude. Next, the rVADM is scaled to absolute VADM with help of compiled data from the GEOMAGIA50 database (<50 ka, Brown et al. (2015)) and from the International Association of Geomagnetism and Aeronomy (IAGA) Absolute Paleointensity (PINT) database (>50 ka, Biggin et al. (2010)), noted as VADM_{DB}. The scaling factor p is obtained by taking the ratio of absolute VADM_{DB} and relative rVADM averages for each record:

$$p = \overline{VADM_{DB}} / \overline{rVADM} \tag{S2}$$

This scaling factor provides the initial calibration of rVADM to VADM. When comparing the distributions of the VADM_{DB} and VADM=p*rVADM, they may not be well overlapped. To further tune the scaling, we introduced two parameters: the shape factor a and position factor b, where a controls the amplitude and b shifts the VADM mean value. Without b, the scaled VADM values sometimes fluctuate in an abnormally large range. The final scaled VADM is calculated in the following way:

$$f(VADM) = a * VADM + b \tag{S3}$$

a and b are obtained iteratively by minimizing the difference (E) of histogram distributions between absolute VADM and f(VADM), with a=1 and b=0.1 as initial values:

$$E = \sum_{i=1}^{k} \left(Hist_i(VADM_{DB}) - Hist_i(f(VADM))\right)^2 \tag{S4}$$

The $Hist_i$ distribution is defined as

$$Hist_i = \frac{n_i}{N} \tag{S5}$$

$$\text{and} \quad \sum_{i=1}^{k} Hist_i = 1 \tag{S6}$$

with bin width of 0.5×10^{22} Am^2, where k is the total number of bins, n_i is the number of values that fall into the ith bin, and N is the total number of values for the studied time period.

The VADMs compiled from the two databases are unevenly distributed in time (Fig. S1a). Therefore, we take the average VADM value for every 100 yrs interval to represent the absolute field intensity for that interval (Fig. S1c). The resulting distribution of VADM is shown in Fig. S1d. Finally, the absolute field intensity is derived by

$$F = \frac{f(VADM)\mu_0}{4\pi r^3\sqrt{1+3\,cos^2\left(\frac{\pi}{2}-\lambda_S\right)}} \tag{S7}$$

An example calibration of RPI to F for core MD07-3076 is shown in Fig. S2.

Declination records of the studied cores were simply rotated to a mean value of zero over the time interval used for the modeling, excluding transitional values defined by Fisher (1953) statistics as directions outside of a 35° circle around the geocentric axial dipole. We performed a test to check the effect of the threshold value 35° vs. the more commonly used value of 45° on the declination scaling (Fig. S3). The two examples, records MD98-2181 and PLC08 show that these two threshold values do not change our declination calibrations. For all our records, the maximum difference in calibration between using 35° and 45° as a threshold is less than 3 degrees. Applying the 35° threshold excludes shallow inclinations and/or large transitional declinations and prevents from introducing a trend in the scaled declination record.

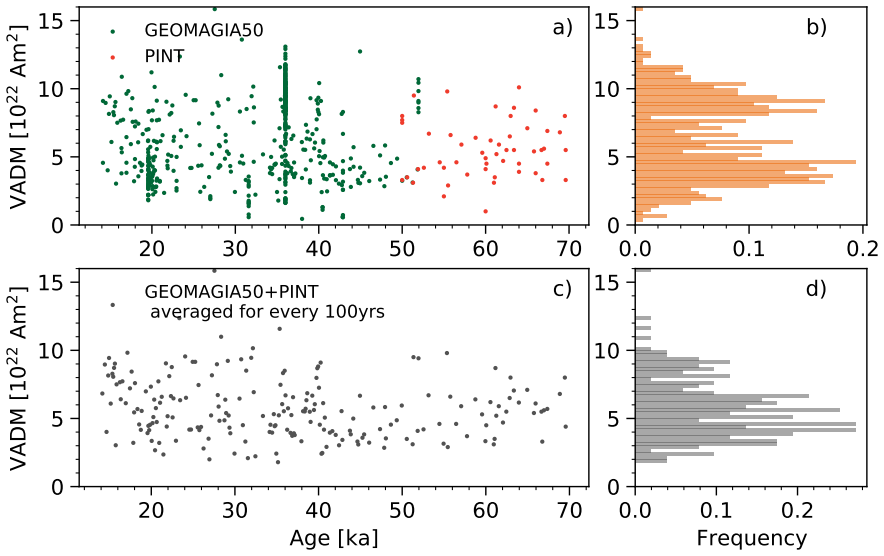

Figure S1: a) Virtual axial dipole moment (VADM) compiled from the GEOMAGIA50 database (<50 ka, green, Brown et al. (2015)) and from the International Association of Geomagnetism and Aeronomy (IAGA) Absolute Paleointensity (PINT) database (>50 ka, red, Biggin et al. (2010)); b) The histogram shows the distribution of VADM values from the two databases for the time interval between 15 and 70 ka in bins of 0.5×10^{22} Am^2; c) VADM values averaged in 100 yr intervals; d) Distribution of values from the 100 yr averaged VADMs for the studied period in bins of 0.5×10^{22} Am^2.

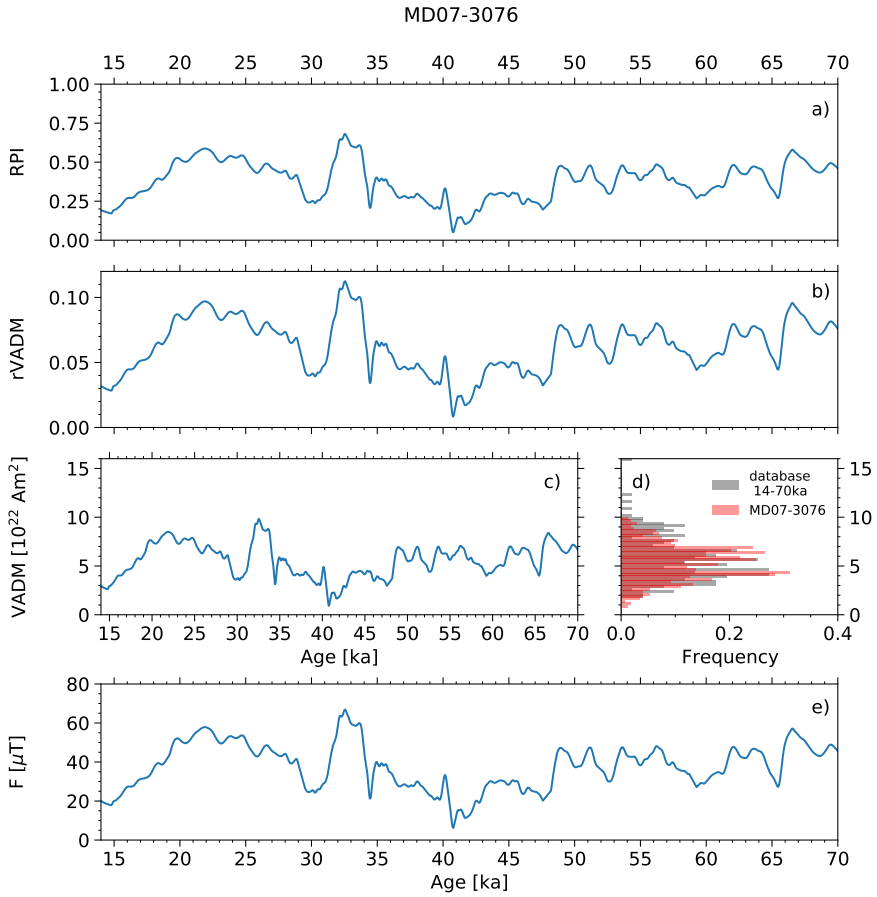

Figure S2: Example of converting relative paleointensity (RPI) of core MD07-3076 to absolute field intensity F. a) RPI; b) Relative virtual axial dipole (rVADM) calculated from RPI following Eq. S1; c) The VADM of core MD07-3076 is derived by minimizing the histogram differences with the absolute VADM values from the databases in Fig. S1, Eqns. S3 and S4; d) VADM distribution histogram of core MD07-3076 (red) with the minimum deviation to the absolute VADM distribution from the two databases (grey); e) The field intensity of core MD07-3076 is calculated following the previous steps and Eq. S7.

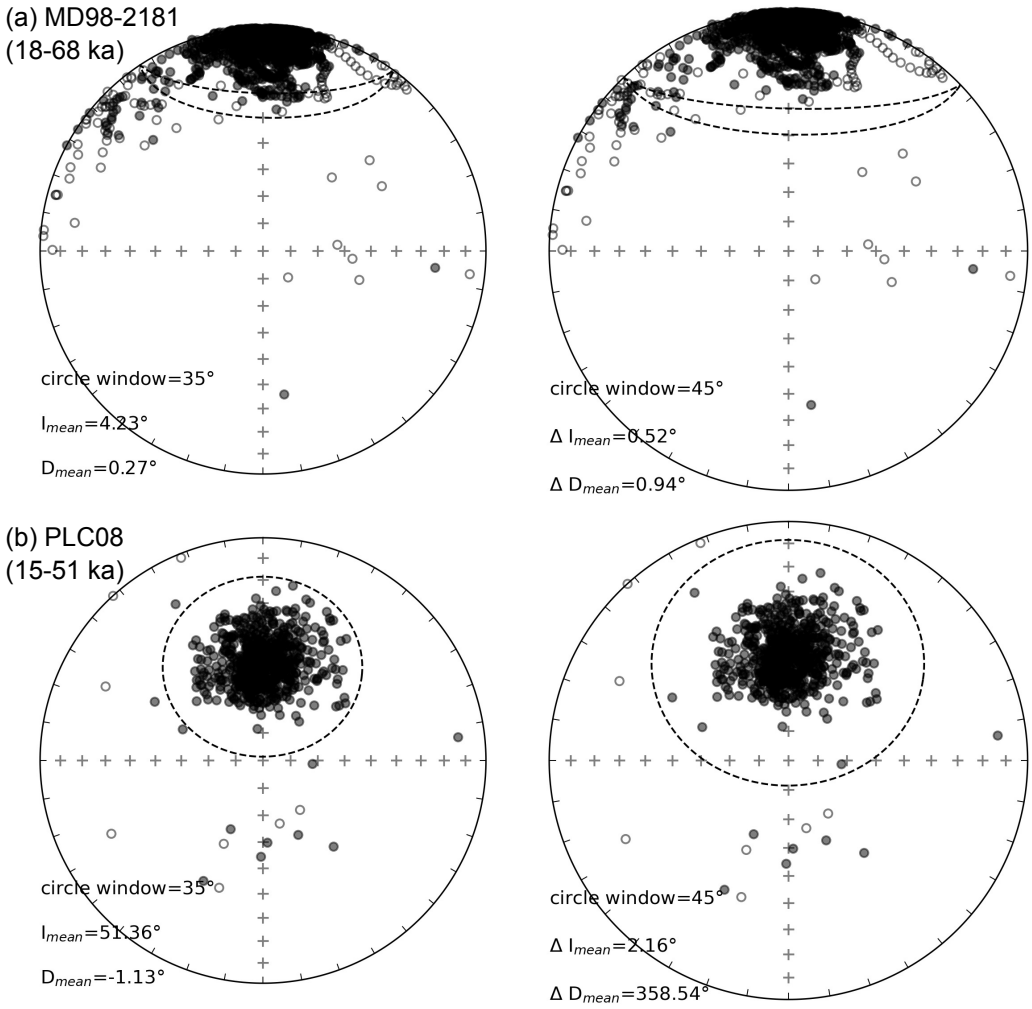

Figure S3: Since the sediment cores were not oriented in azimuth, we obtained oriented declinations by rotating all values to a common mean value of 0°. Averaging was done by applying Fisher (1953) statistics to all directions falling inside a circle of 35° around the expected dipole. We tested the threshold of 35° and the more common value of 45° for identifying transitional directions that are excluded in calculating the mean (35° and 45° in the left and right column, respectively). The two records, MD98-2181 (a) and PLC08 (b) show very small differences in the mean declination.

S2 Updated age models

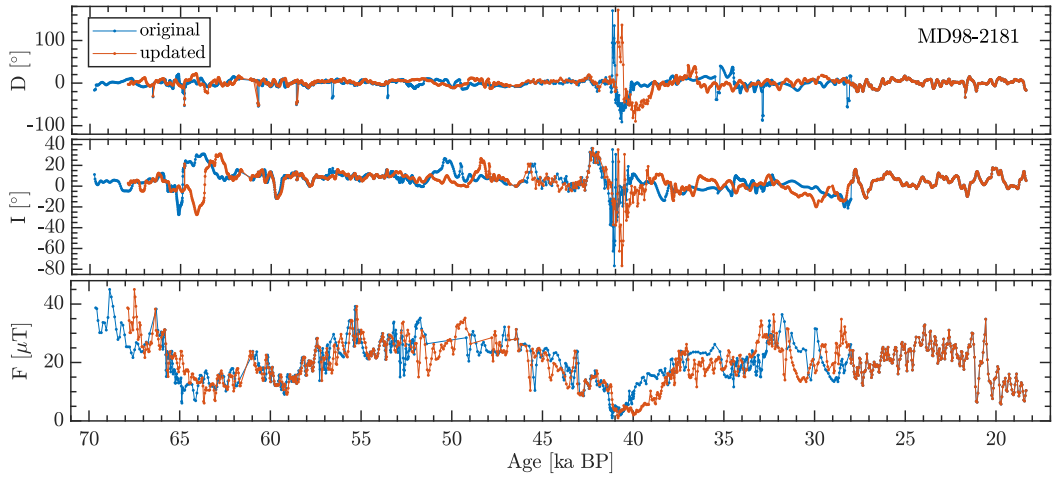

Figure S4: The age model of record MD98-2181 is updated only for the period beyond 28 ka, dated with oxygen isotope stratigraphy, to GICC05 age model following Obrochta et al. (2014). The age model for the period from 28 ka to present, which is based on the revised calibrated radiocarbon dating (Khider et al., 2014), is kept.

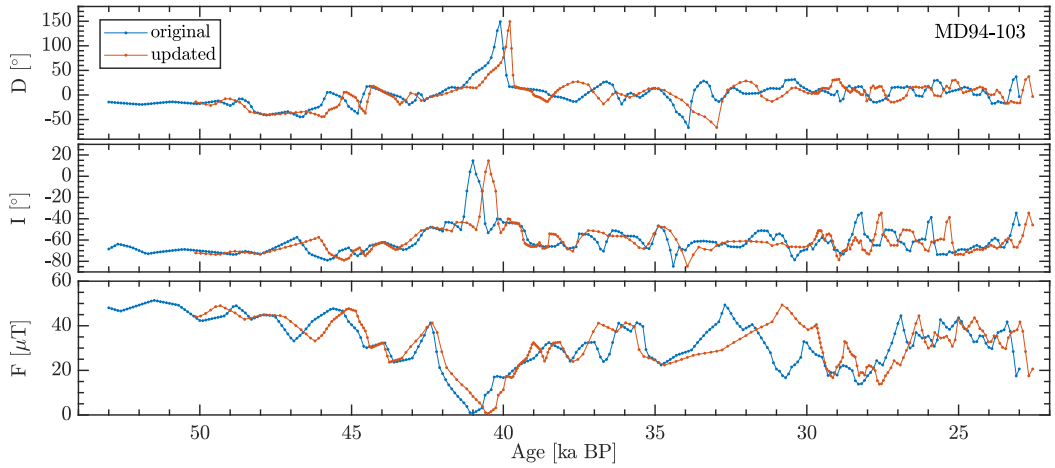

Figure S5: The age model of record MD94-103 is updated according to Anderson et al. (2021). The record is aligned to the Antarctic temperature record on the AICC2012 timescale, and further tuned based on the existence of Antarctic Isotope Maximum (AIM) event type warmings.

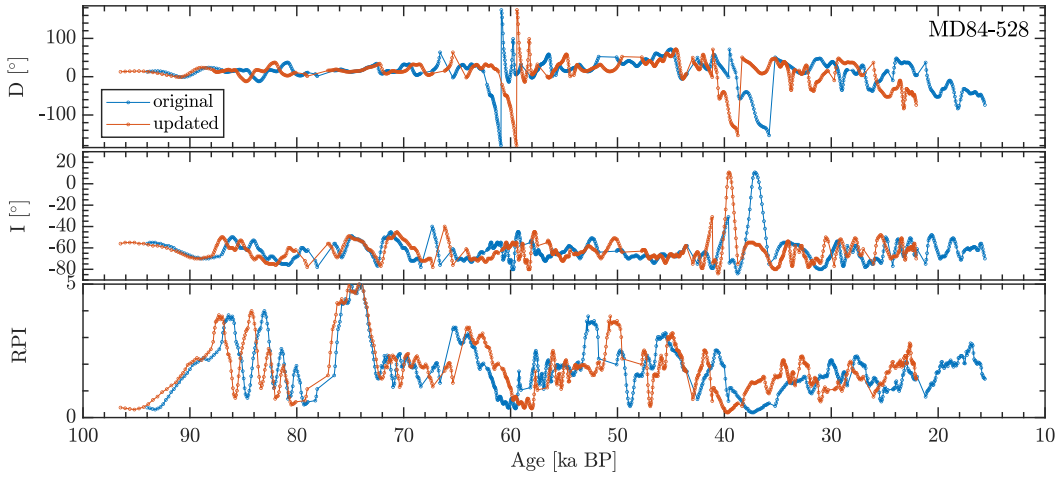

Figure S6: The age model of record MD84-528 (Tric et al., 1992) is updated from the SPECMAP δ^{18}O reference curve (Imbrie et al., 1984; Martinson et al., 1987) to U/Th calibrated δ^{18}O event boundaries from Thompson & Goldstein (2006). Linear interpolation between MIS stage boundaries is applied.

S3 Selection of smoothing parameters

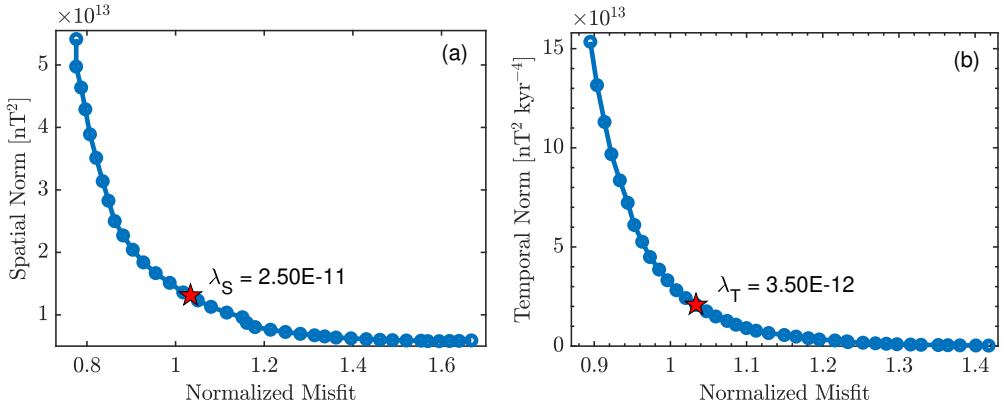

Figure S7: The regularization combines measures of spatial and temporal complexities of the model with the misfit between data and model predictions in the objective functional of the inversion. The smoothing parameters are chosen in the "knees" (red star) of the L–curves, which describe the trade–off between the misfit and the norms measuring the (a) spatial and (b) temporal complexity of the model.

S4 Smoothing time analysis

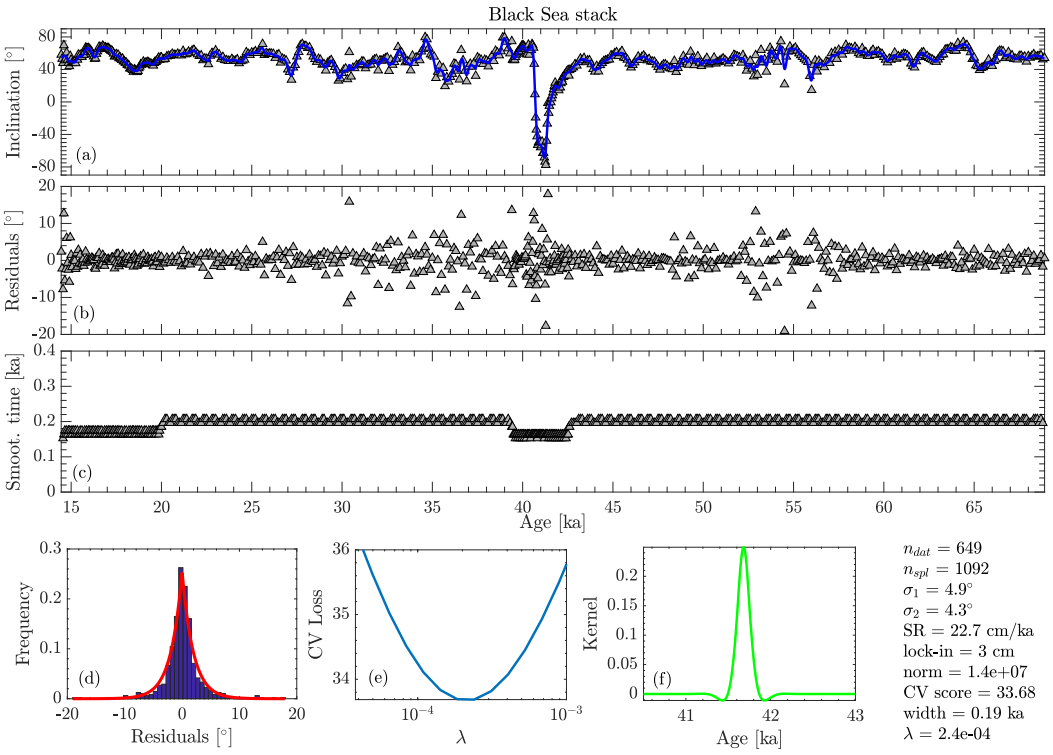

Figure S8: Example of the spline analysis of the inclination record from the Black Sea. Details on the methods can be found in Panovska et al. (2012). (a) Data time series (gray triangles) and penalized least square spline fit (blue curve); (b) time series of residuals; (c) time series of the smoothing width; (d) histogram of residuals (normalized to the unit area) with a Laplacian distribution (red curve); (e) Cross Validation (CV) score as a function of the smoothing parameter λ (blue curve). The minimum of the CV score determines the choice of λ. The x-axis on this subplot is given in logarithmic scale; (f) an example of kernel function estimated at the central point of the same record, which diagnoses the temporal resolution. The width refers to a full width at half maximum of this kernel function. This width is estimated at each internal point of the record (as in c) and only the mean is reported for each record (width). Information about the number of data (ndat), number of splines (nspl), the L1 measure of misfit (σ_1), the L2 measure of misfit (σ_2), mean sedimentation rate (SR), assumed lock-in depth (lock-in), the norm measuring the model roughness (norm), the value of the CV minimum (CV score), the mean width of the resolving kernel (width), and the corresponding smoothing parameter (λ) are provided in the label.

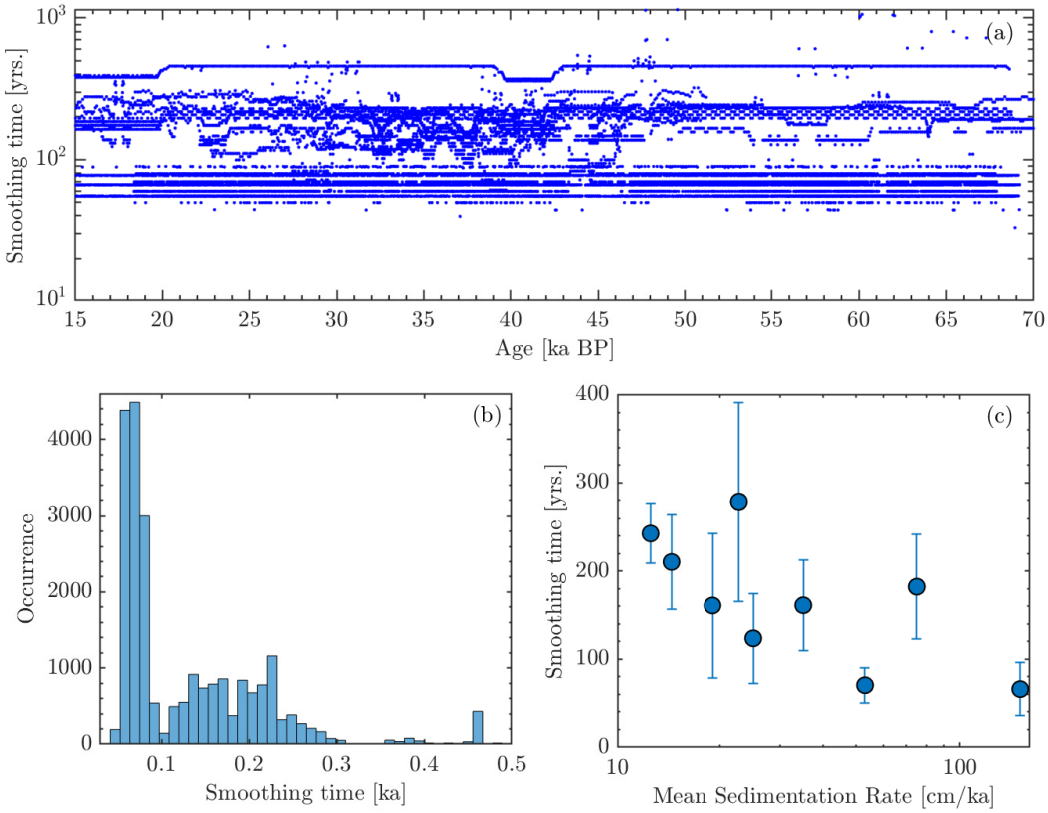

Figure S9: Summary of the analysis for estimating the time resolution of sediment records that constrained the GFFSS70 model. (a) Time variations of the smoothing time of all records and components, (b) Histogram of the smoothing times, and (c) Smoothing times by individual records (mean value and one standard deviation) as a function of mean sedimentation rate.

S5 Declination uncertainties

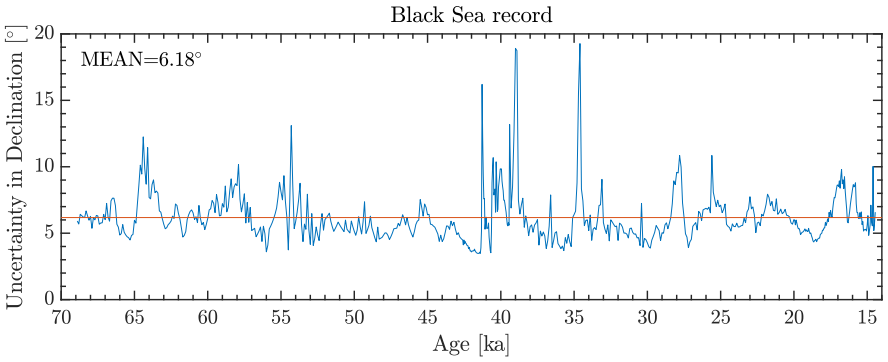

Figure S10: Changes of declination uncertainty in the Black Sea record considering the inclination variations and α_{95} of 8.5 degrees. The mean value, 6.18°, is taken in the model.

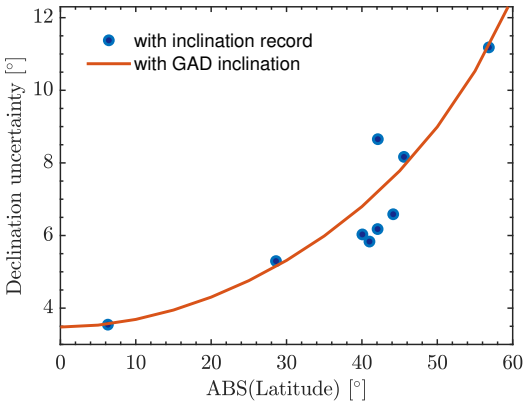

Figure S11: Dependence of uncertainty estimates for declination on the latitude of each record that constrains the GGFSS70 model. Declination uncertainties are estimated by considering inclination variations and averaged over the studied period. The solid line represents the values estimated using the same equation but GAD-expected inclinations for each location.

S6 Model predictions

The following nine figures present the model predictions of declination D, inclination I and intensity F for each of the paleomagnetic sediment record that constrain the GGFSS70 model as red curves together with the data shown by black dots.

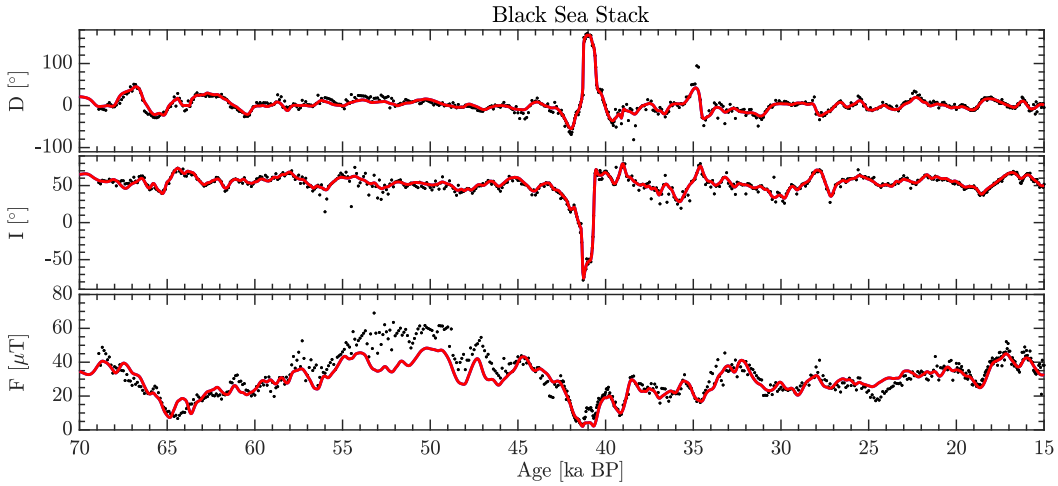

Figure S12: GGFSS70 model predictions and the Black Sea record.

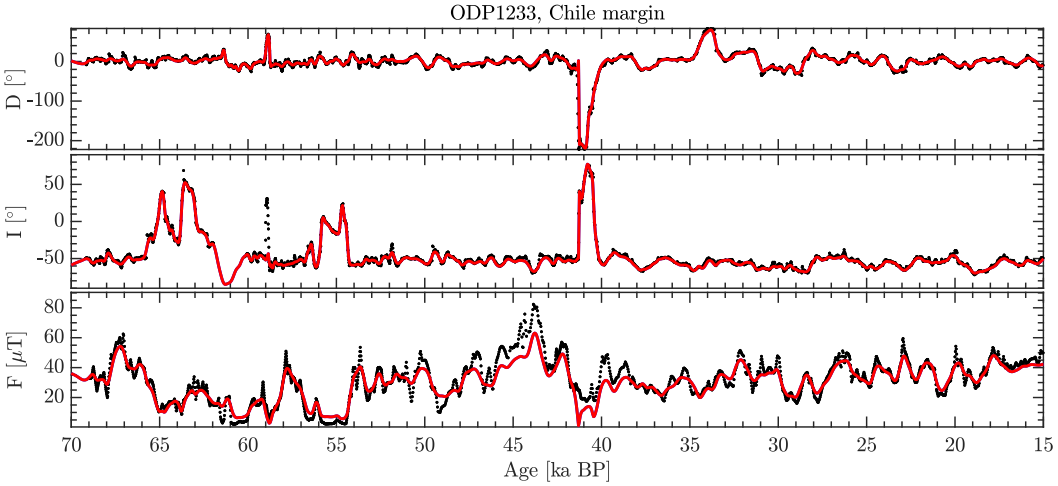

Figure S13: GGFSS70 model predictions and the ODP1233 record.

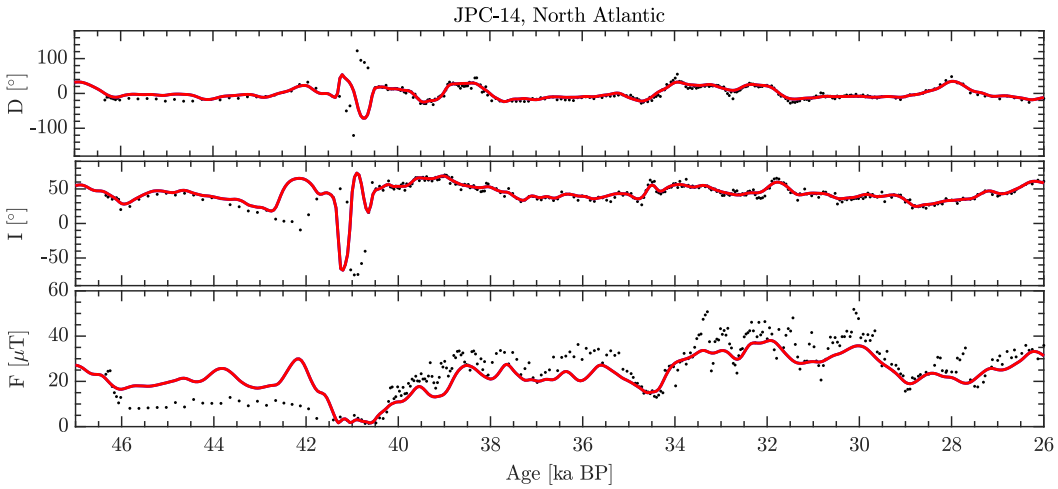

Figure S14: GGFSS70 model predictions and the JPC-14 record.

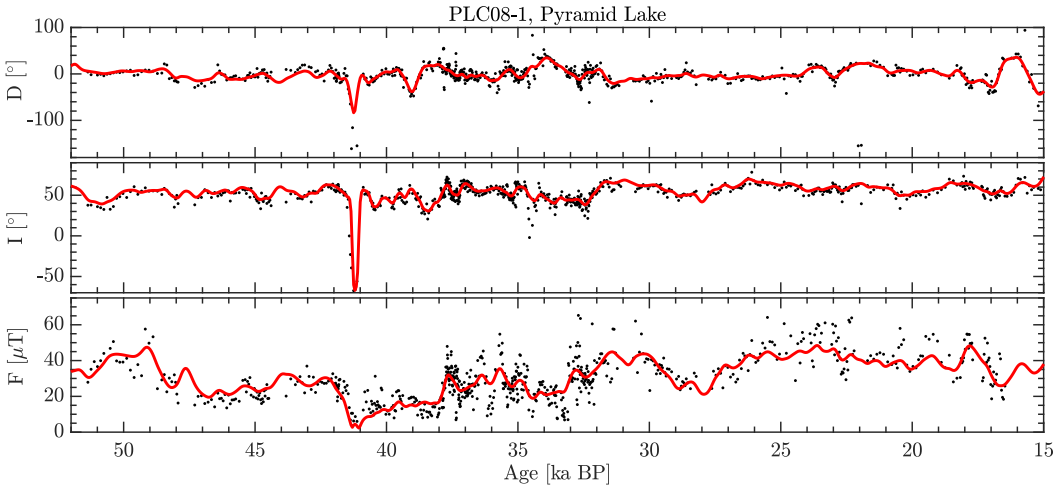

Figure S15: GGFSS70 model predictions and the PLC08-1 record.

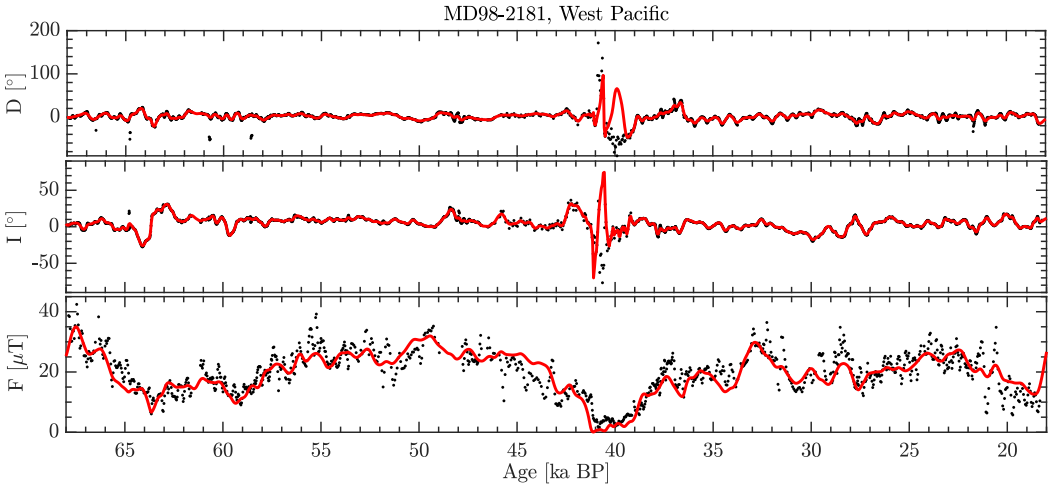

Figure S16: GGFSS70 model predictions and the MD98-2181 record.

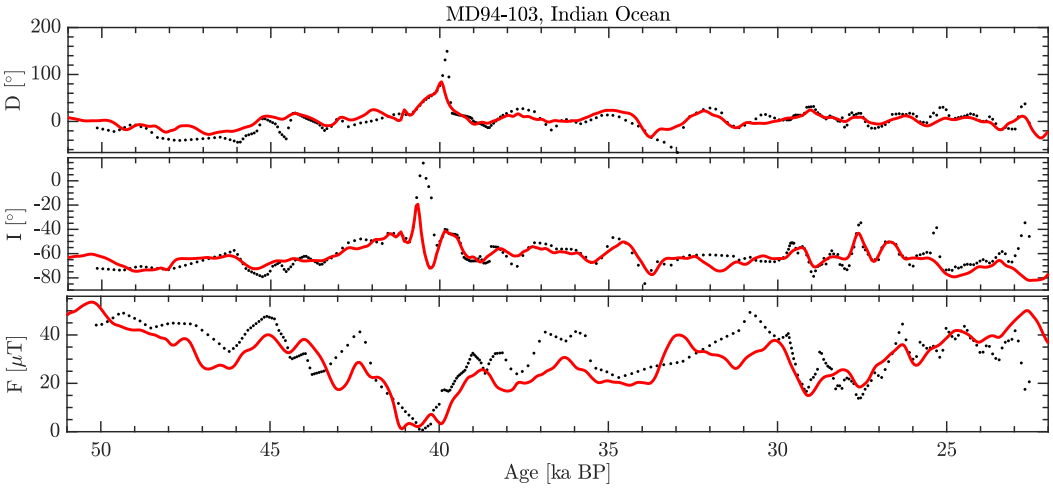

Figure S17: GGFSS70 model predictions and the MD94-103 record.

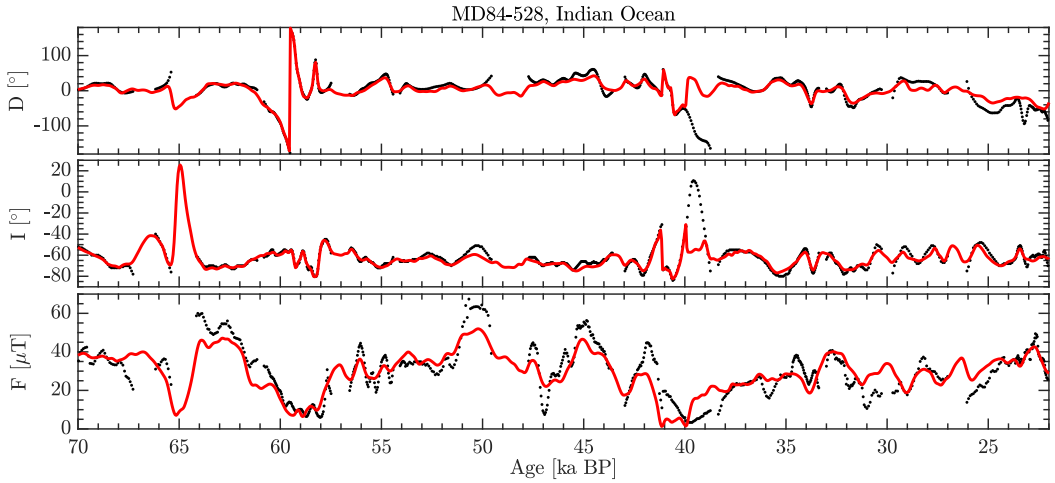

Figure S18: GGFSS70 model predictions and the MD84-528 record.

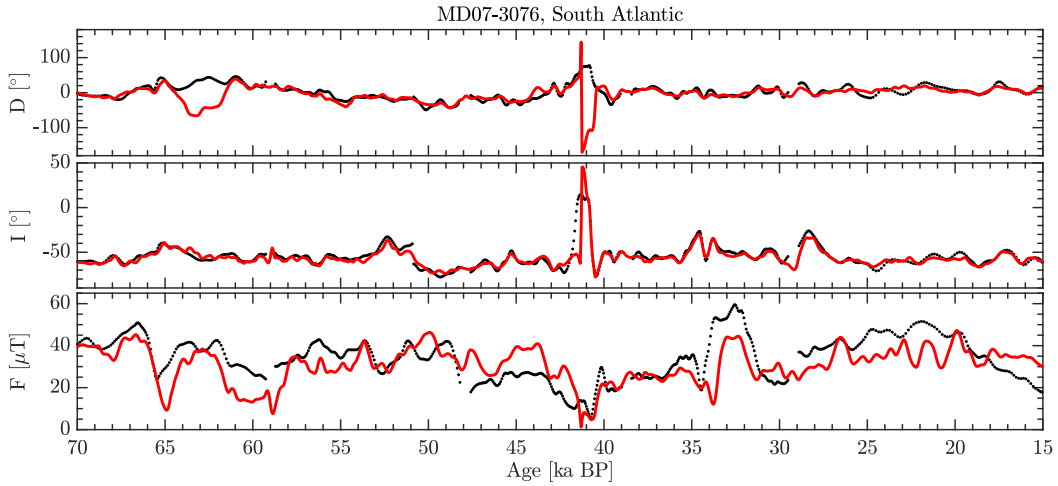

Figure S19: GGFSS70 model predictions and the MD07-3076 record.

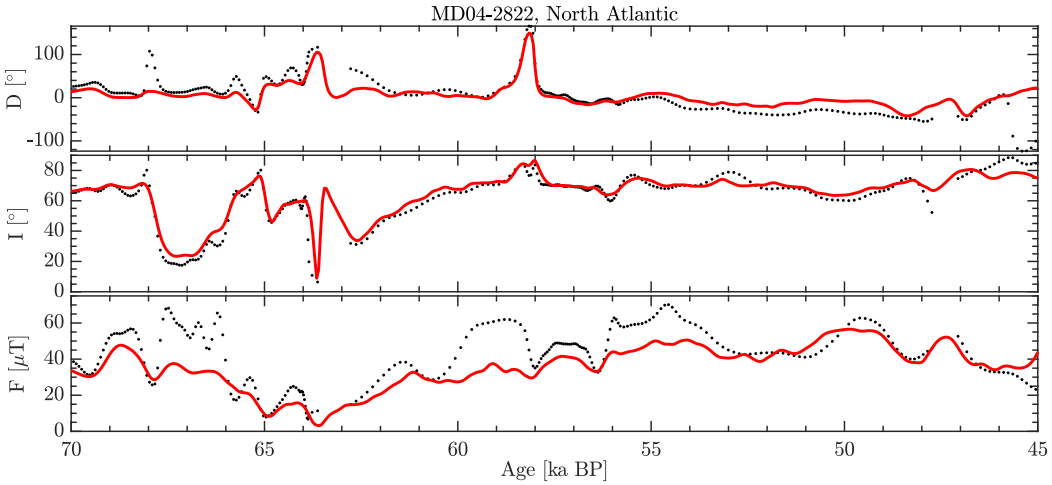

Figure S20: GGFSS70 model predictions and the MD04-2822 record (over the time period used in the model).

S7 Time variations of model coefficients

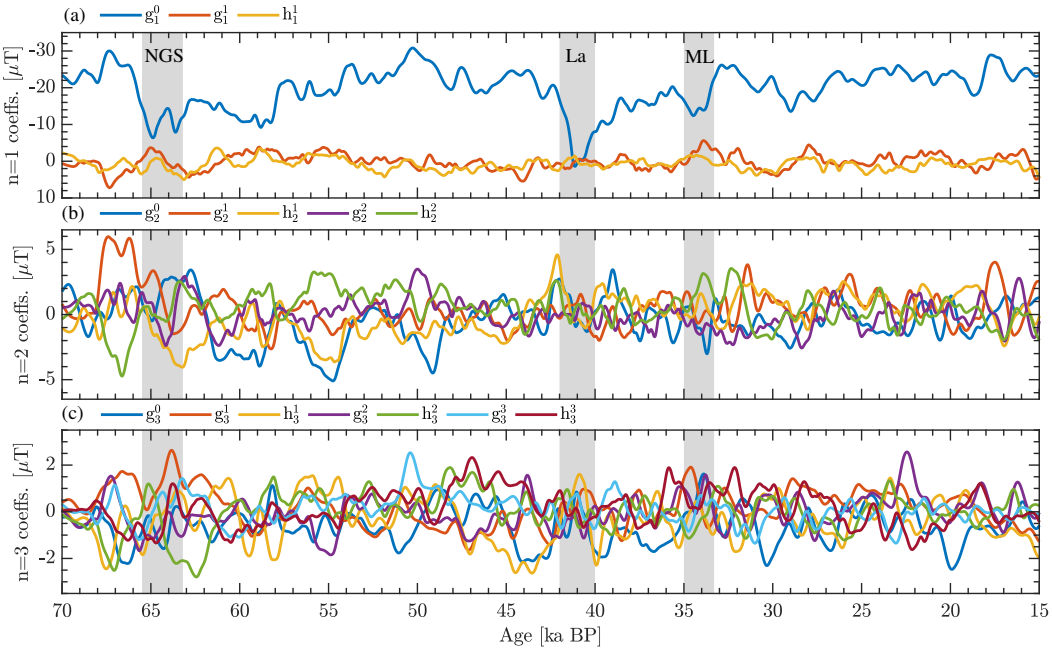

Figure S21: Time evolution of (a) dipole, (b) quadrupole, and (c) octupole coefficients of the GGFSS70 model. Note the reverse y–direction for the dipole coefficients. Gray areas indicate the three geomagnetic excursions noted at the top: NGS-Norwegian-Greenland Sea, La-Laschamps, and ML-Mono Lake excursion.

Table S1: Comparisons of the GGFSS70 ADM with GGF100k (Panovska et al., 2018) and LSMOD.2 (Korte et al., 2019) values. Minimum, maximum, mean and standard deviation values are listed.

ADM	Validation period [kyr]	Analyzed period [kyr]	MIN [10^{22}Am^2]	MAX [10^{22}Am^2]	MEAN±STD [10^{22}Am^2]
GGFSS70	15–70	15–70	9.8e-4	7.97	5.09±1.48
		30–50	9.8e-4	7.69	4.77±1.62
GGF100k	0–100	0–100	2.44	9.89	6.78±1.21
		15–70	2.44	9.15	6.60±1.26
		30–50	2.44	8.32	6.07±1.35
LSMOD.2	30–50	30–50	0.29	8.04	5.18±1.82

S8 Mono Lake/Auckland excursion

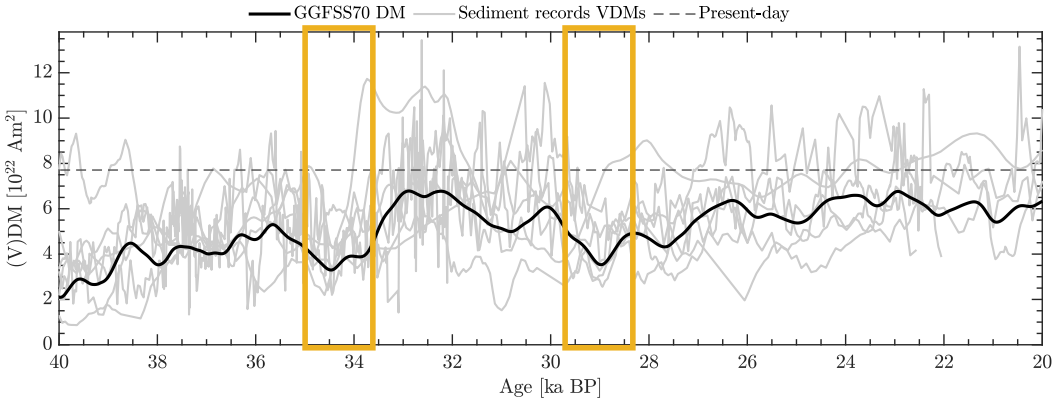

Figure S22: Time variations of the VDMs estimated from the nine individual records that constrained the GGFSS70 model (light grey curves), dipole moment of GGFSS70 model and present-day are plotted over the period 40 to 20 ka BP. The orange blocks denote the periods of the two intensity lows, at ∼34 ka and ∼29 ka, observed in the data and also captured by the model.

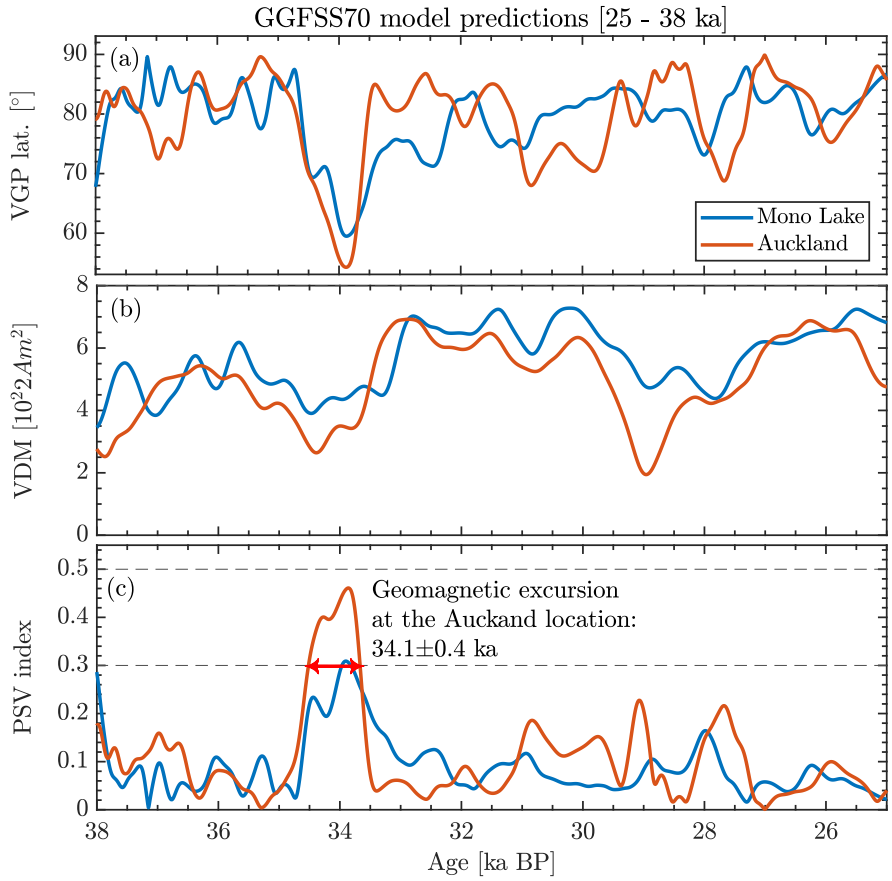

Figure S23: Field predictions from the GGFSS70 model (over the period 25–38 ka) at the locations of Mono Lake (38°N, 119°W) and Auckland volcanic field (37°S, 175°E): VGP latitude (a); VDM (b); and the PSV index (c). The dashed lines (in c) are the threshold value of the PSV index of 0.5 characteristic for transitional events (excursions and reversal), and 0.3, the more conservative value, which has never been exceeded in the recent models that cover periods with no transitional events. The peak PSV index at the Auckland location results from simultaneous lower field intensity and VGP latitude about 34 ka. Considering the 0.3 threshold, as the 0.5 is not reached, the excursion is confined in the 34.1±0.4 ka period. On the other hand, the GGFSS70 model produce weakly increased, but not excursional, values at the Mono Lake location.

S9 Regional variations of VDM, VGP and PSV index

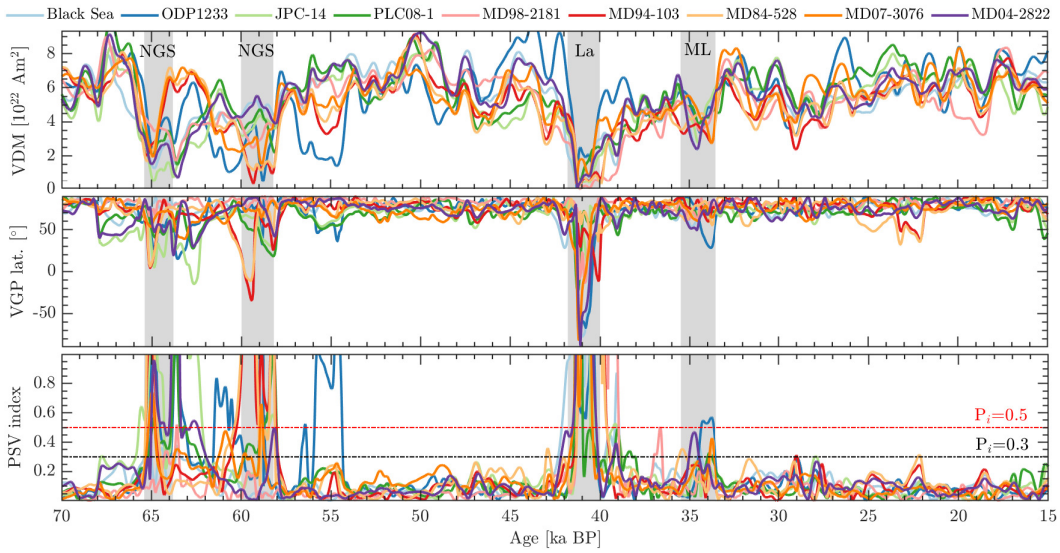

Figure S24: Model predictions at records locations expressed as VDM, geomagnetic pole latitude, and PSV index estimated from the previous two quantities over the 15–70 ka period. The threshold values of the PSV index of 0.5 (0.3), which shows transitional events, is plotted as horizontal dash–dotted line. The y-axis is cut at 1 for better visualization of variations closed to the threshold. Gray areas indicate the three geomagnetic excursions noted at the top: NGS-Norwegian-Greenland Sea, La-Laschamps, and ML-Mono Lake excursion.

S10 Ages and durations of excursions

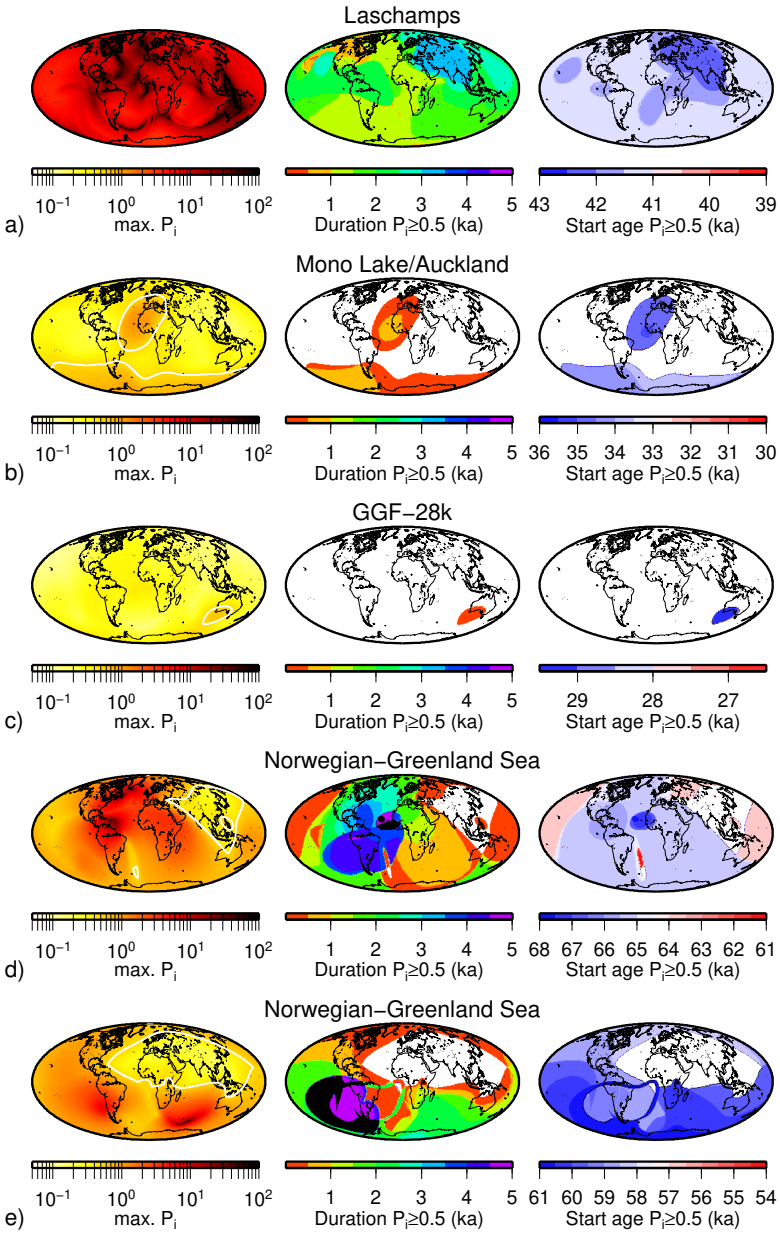

Figure S25: Maximum P_i, duration, and starting age of excursions with $P_i \geq 0.5$ in the GGFSS70 model: (a) Laschamps excursion; (b) Mono Lake/Auckland excursion; (c) The GGF-28k event found in the GGF100k model; (d) Norwegian-Greenland Sea excursion (about 65 ka); and (d) Norwegian-Greenland Sea excursion (about 60 ka). White contour line in maximum P_i plots is 0.5. Duration and starting age are estimated for areas with $P_i \geq 0.5$, otherwise left white. For all these periods, the P_i exceeds the 0.5 threshold over smaller or larger region, and the whole globe for the Laschamps excursion.

S11 Power spectrum comparisons

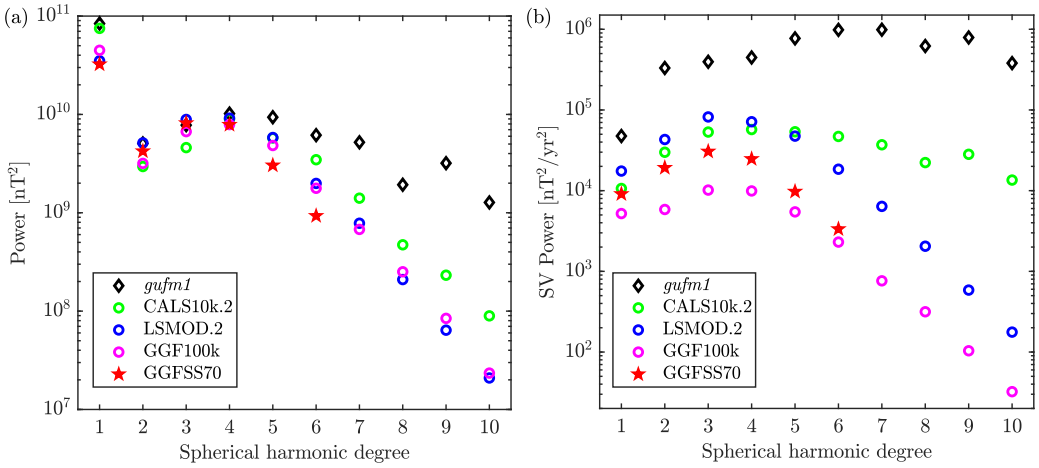

Figure S26: Comparison of the spherical harmonic spectra of the time-averaged geomagnetic field and its secular variation at the core-mantle boundary. Models: *gufm1* (Jackson et al., 2000); CALS10k.2 (Constable et al., 2016); LSMOD.2 (Korte et al., 2019), GGF100k (Panovska et al., 2018), and GGFSS70 (this study).

S12 Synthetic tests

We have performed synthetic tests to assess the level of resolved features with our limited data set. The synthetic data were obtained using the numerical simulation model 'h' by Glatzmaier et al. (1999) that has an imposed CMB heat flux inferred from simulations of mantle convection and large–scale seismic tomography of the lowermost mantle. Two data sets were created and tested: Originally Distributed Data (ODD) and Equally Distributed Data (EDD). The ODD set contains synthetic data at the locations/times used in the GGFSS70 model. The EDD case has the same locations, but all records have the three components equally distributed in time, every 50 years. Both synthetic data sets were inverted in the same way as the original data.

The synthetic tests (Fig. S27) show that the resolved structure vary in time: (a) the EDD synthetic model better resolves the field in comparison with the ODD model clearly showing the effect of inverting the EDD data; (b) Both synthetic models have overlapping powers that agree with the numerical model up to degree 4; (c) 62 ka is an epoch when there is a lower number of data (visible in the temporal data distribution) and both synthetic models resolve structures up to degree 3. These tests show that the effective resolution of the GGFSS70 model is up to degree 3-4 and it varies in time. The maps of the B_r field at the CMB (Fig. S28) also show that large scale-structure (degree 3-4) are resolved with the dataset that constrained the GGFSS70 model.

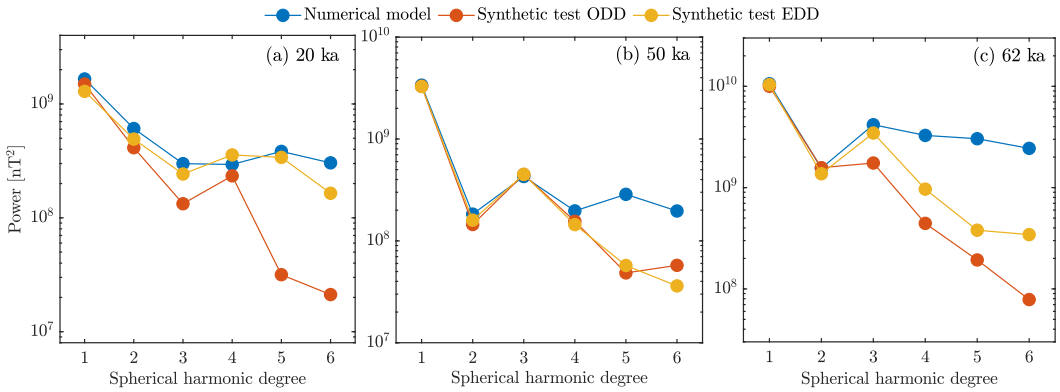

Figure S27: Energy spectra at the CMB at 20 ka (a), 50 ka (b), and 62 ka (c), for the synthetic models constrained with two different data sets: Equally Distributed Data (EDD) and Originally Distributed Data (ODD) compared to the spectrum of the numerical model (Glatzmaier et al., 1999) used to create the synthetic series.

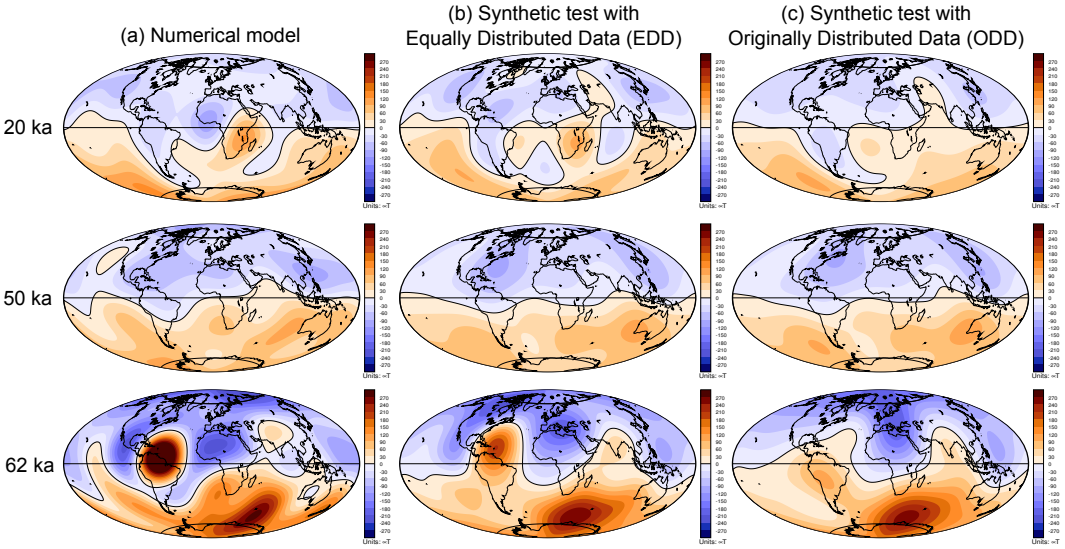

Figure S28: Maps of the B_r component at the CMB up to SH degree 6 from the numerical simulation model and the synthetic models obtained with Equally Distributed Data (EDD) and Originally Distributed Data (ODD) sets compared to the numerical model (Glatzmaier et al., 1999) used to create the synthetic series. Large-scale structures (up to degree 3-4) are reconstructed with the data set that constrained the GGFSS70 model.

S13 Dipole/Non–dipole energy comparisons

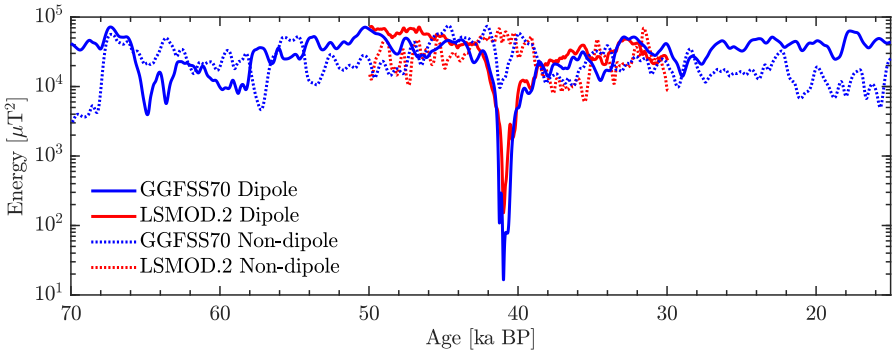

Figure S29: Comparison of the dipole and non–dipole power at the CMB from the GGFSS70 (70–15 ka) and LSMOD.2 (50–30 ka) model.

S14 CMB morphology during excursions

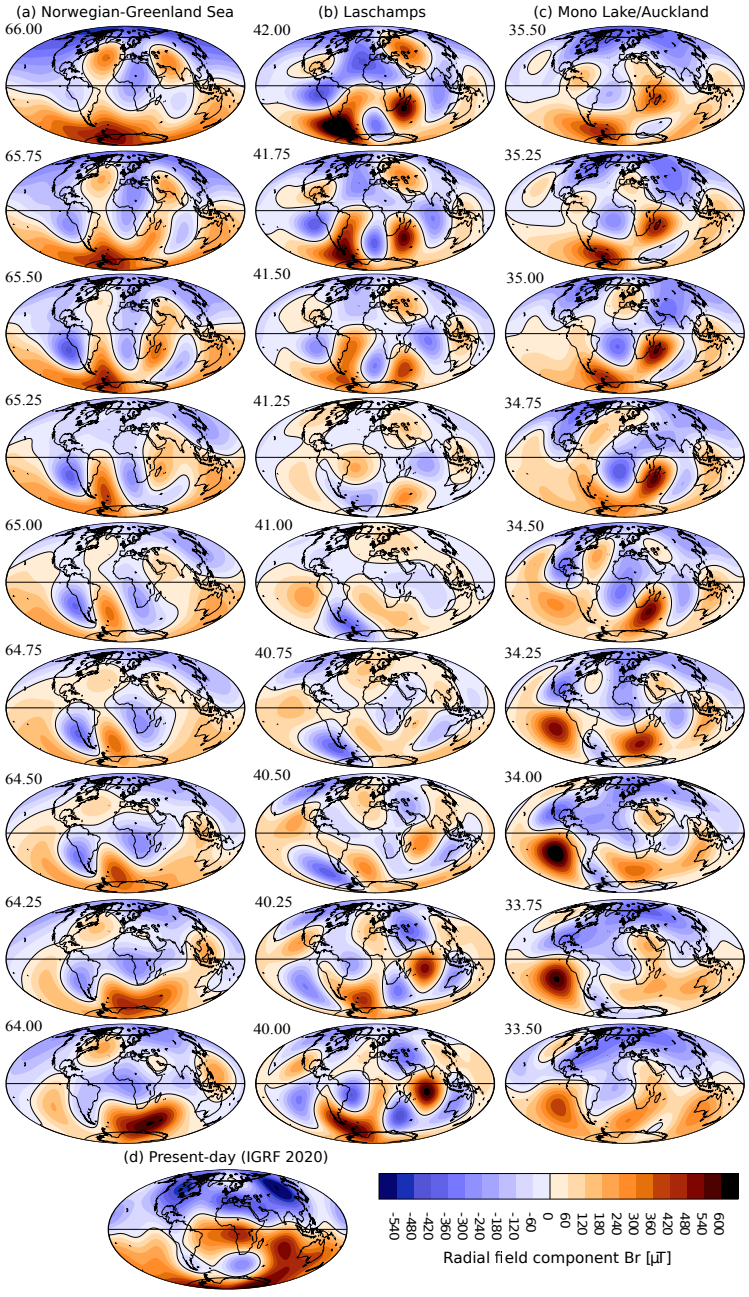

Figure S30: Maps of the radial component of the magnetic field (B_r, in μT) at the core–mantle boundary at intervals of 250 years covering the period of (a) Norwegian–Greenland Sea excursion; (b) Laschamps excursion; (c) Mono Lake/Auckland excursion; (d) Present–day field predicted from the IGRF13 model (truncated to degree 6).

References

Anderson, H. J., Pedro, J. B., Bostock, H. C., Chase, Z., & Noble, T. L. (2021). Compiled Southern Ocean sea surface temperatures correlate with Antarctic Isotope Maxima. Quatern. Sci. Rev., 255, 106821. doi: 10.1016/j.quascirev.2021.106821

Biggin, A. J., McCormack, A., & Roberts, A. (2010). Paleointensity database updated and upgraded. EOS Trans. Am. Geophys. Union, 91(2), 15. doi: 10.1029/2010EO020003

Brown, M. C., Donadini, F., Korte, M., Nilsson, A., Korhonen, K., Lodge, A., ... Constable, C. G. (2015). GEOMAGIA50.v3: 1. General structure and modifications to the archeological and volcanic database. Earth Planets Space, 67:83. doi: 10.1186/s40623-015-0232-0

Constable, C. G., Korte, M., & Panovska, S. (2016). Persistent high paleosecular variation activity in southern hemisphere for at least 10 000 years. Earth Planet. Sci. Lett., 453, 78-86.

Fisher, R. A. (1953). Dispersion on a sphere. Proc. R. Soc. Lon. A, 217, 295-305.

Glatzmaier, G. A., Coe, R. S., Hongre, L., & Roberts, P. H. (1999). The role of the earth's mantle in controlling the frequency of geomagnetic reversals. Nature, 401, 885-890.

Imbrie, J., Hays, J. D., Martinson, D. G., McIntyre, A., Mix, A. C., Morley, J. J., ... Shackleton, N. J. (1984). The orbital theory of Pleistocene climate: Support from a revised chronology of the marine δ^{18}O record. In A. L. Berger, J. Imbrie, J. Hays, G. Kukla, & B. Saltzmen (Eds.), Milankovitch and Climate, Part I (Vol. 126, p. 269-305). Reidel.

Jackson, A., Jonkers, A. R. T., & Walker, M. R. (2000). Four centuries of geomagnetic secular variation from historical records. Phil. Trans. R. Soc. Lond. A, 358, 957-990.

Khider, D., Jackson, C. S., & Stott, L. D. (2014). Assessing millennial-scale variability during the Holocene: A perspective from the western tropical Pacific. Paleoceanography, 29, 143-159. doi: 10.1002/2013PA002534

Korte, M., Brown, M. C., Panovska, S., & Wardinski, I. (2019). Robust characteristics of the Laschamps and Mono Lake geomagnetic excursions: Results from global field models. Front. Earth Sci., 7. doi: 10.3389/feart.2019.00086

Martinson, D. G., Pisias, N. G., Hays, J. D., Imbrie, J., Moore Jr., T. C., & Shackleton, N. J. (1987). Age dating and the orbital theory of the Ice Ages: Development of a high-resolution 0 to 300,000-year chronostratigraphy. Quatern. Res., 27, 1-29.

Obrochta, S. P., Yokoyama, Y., Morén, J., & Crowley, T. J. (2014). Conversion of GISP2-based sediment core age models to the GICC05 extended chronology. Quat. Geochronology, 20, 1-7.

Panovska, S., Constable, C. G., & Korte, M. (2018). Extending global continuous geomagnetic field reconstructions on timescales beyond human civilization. Geochem. Geophys. Geosyst., 19. doi: 10.1029/2018GC007966

Panovska, S., Finlay, C. C., Donadini, F., & Hirt, A. M. (2012). Spline analysis of Holocene sediment magnetic records: Uncertainty estimates for field modelling. J. Geophys. Res., 117, B02101. doi: 10.1029/2011JB008813

Thompson, W. G., & Goldstein, S. L. (2006). A radiometric calibration of the SPECMAP timescale. Quat. Sci. Rev., 25, 3207-3215. doi: 10.1016/j.quascirev.2006.02.007

Tric, E., Valet, J.-P., Tucholka, P., Paterne, M., Labeyrie, L., Guichard, F., ... Fontugne, M. (1992). Paleointensity of the geomagnetic field during the last 80 000 years. J. Geophys. Res., 97(B6), 9337-9351.